Supporting Information

Metal Free Sulfonate/Sulfate Functionalized Carbon Nitride for Direct Conversion of Glucose to Levulinic Acid

Pawan Kumar,[1+] Ali Shayesteh Zeraati,[1+] Soumyabrata Roy,[2] Kristen A. Miller,[2] Aiguo Wang,[1] Lawrence B. Alemany,[3] Tareq A. Al-Attas,[1] Dhwanil Trivedi,[1] Pulickel M. Ajayan,[2] Jinguang Hu,[1]* and Md Golam Kibria[1]*

[1]*Department of Chemical and Petroleum Engineering, University of Calgary, 2500 University Drive, NW Calgary, Alberta, Canada*

[2]*Department of Materials Science and NanoEngineering, Rice University, 6100 Main St., Houston, TX 77030, USA*

[3]*Department of Chemistry and Shared Equipment Authority, Rice University, Houston, TX 77005, United States*

*Jinguang Hu (jinguang.hu@ucalgary.ca)

*Md. Golam Kibria (md.kibria@ucalgary.ca)

[+]P.K. and A.S.Z. contributed equally to this paper

Number of pages: 33

Number of figures and schemes: 18

Number of tables: 3

Contents

1.0 Experimental details	**Page S3**
1.1 Reagents and Materials	**Page S3**
1.2 Physicochemical characterization	**Page S3**
2.0 Synthesis of materials	**Page S6**
2.1 Synthesis of sulfonate/sulfate functionalized carbon nitride (CNS)	**Page S6**
2.2 Synthesis of graphitic carbon nitride, CN	**Page S6**
2.3 Synthesis of sulfonated graphitic carbon nitride, SGCN	**Page S7**
3.0 Glucose to levulinic acid conversion experiments	**Page S7**
4.0 Additional catalyst characterization	
4.1 XRD Analysis	**Page S10**
4.2 Raman Analysis	**Page S11**
4.3 Dispersibility, Zeta Potential (ζ) and average particle size (d.nm)	**Page S12**
4.4 Thermogravimetric analysis/differential scanning calorimetry	**Page S15**
5.0 UV-Vis and XPS valence band spectra	**Page S19**
Figures	
Figure S1. FE-SEM and Elemental mapping of the CN	**Page S8**
Figure S2. FE-SEM image and Elemental mapping of the CNS	**Page S9**
Figure S3. HR-TEM images of CNS and SAED pattern of CNS	**Page S10**
Figure S4. X-ray diffraction spectra of CN and CNS	**Page S11**
Figure S5. Digital photograph of CN and CNS	**Page S13**
Figure S6. Apparent zeta potential (ζ) of CN and CNS	**Page S14**
Figure S7. Particle size distribution of CN and CNS	**Page S15**
Figure S8. TGA and DSC thermogram of CN and CNS	**Page S17**
Figure S9. XPS elemental survey scan of CN and CNS	**Page S18**
Figure S10. HR-XPS spectra of CNS in O1s region.	**Page S18**
Figure S11. UV-Vis DRS spectra of CN and CNS.	**Page S20**
Figure S12. Valence band (VB) spectra of CN and CNS.	**Page S21**
Figure S13. FTIR and Raman spectra of recycled CNS catalysts	**Page S21**
Figure S14. GC-MS spectra of glucose hydrothermal conversion products.	**Page S22**
Figure S15. GC-MS spectra of glucose hydrothermal conversion products	**Page S23**
Figure S16. Overlayed ^{1}H NMR spectra of products	**Page S24**
Figure S17. Overlayed ^{1}H NMR spectra of Products	**Page S25**
Figure S18. Zoomed overlayed ^{1}H NMR spectra of products	**Page S26**
Table S1. The yield of various products obtained from the hydrothermal treatment of glucose using CN and CNS as a catalyst at 120 ℃, 150 ℃ and 200 ℃.	**Page S27**
Table S2. Performance of SGCN and CNS for glucose/fructose conversion	**Page S28**
Table S3. Comparison of glucose to LLA conversion with reported catalysts	**Page S29**

1. Experimental details

1.1 Reagent and materials

Dicyandiamide (99%), Ammonium persulfate (98%), and Glucose (96%) were procured from Sigma and used as received. HPLC analysis was done by using HPLC grade Levulinic acid (98%), 5-(hydroxymethyl) furfural HMF (99%), Lactic acid (98%), Acetic acid (98%), Formic acid (95%), Glycolic acid (99%) and Erythrose (75%) received from Sigma. HPLC grade solvents and DI water were used throughout the experiments.

1.2 Physicochemical characterization

The microscopic structural attributes of the materials were determined using field-emission scanning electron microscopy (FESEM), using FEI Quanta 250 FEG field emission SEM, equipped with EDS analysis. The ultrafine structural attributes of the materials were studied using a high-resolution transmission electron microscopy (HR-TEM), recorded on a JEOL JEM-ARM200CF S/TEM operating at an acceleration voltage of 200 KeV. For the preparation of samples, a very dilute suspension of the materials in methanol was made followed by sonication for 2h. Finally, the obtained suspension was dropped on a 300-mesh lacy carbon-coated copper TEM grid and dried under an incandescent lamp. The average particles size and surface charge distribution of CN and CNS catalysts were determined by using dynamic light scattering (DLS) acquired by using Malvern Zetasizer.

MAS NMR spectra were obtained on a 4.7 T spectrometer previously described in detail.[1] Parameters for ^{13}C data acquisition and processing were as previously described[1] except as follows. Cross polarization with 8.5 kHz MAS so that any spinning sidebands are at multiples of 169 ppm from a centerband; 2464 scans (CN) and 1920 scans (CNS) for each of the 18 experiments with different contact times; FIDs processed with 50 Hz (1 ppm) of line broadening. Direct 90°

^{13}C pulse experiment using 10s or 30s relaxation delay; 6336 scans (CN) and 7680 scans (CNS) for each experiment; FIDs processed with 50 Hz (1 ppm) of line broadening. Additional details are in figure captions. Parameters for ^{15}N data acquisition and processing are as follows: CP with 5 kHz MAS and a spectral width of 31,250 Hz (1541 ppm) so that any spinning sidebands are at multiples of 246 ppm from a center band. Cross polarization experiments started with a 2.5-μs, 90° ^{1}H pulse and used the Bruker ramp.100 program for the ramped ^{1}H pulse during the contact time; 32.8-ms FID; 5-s relaxation delay; 30,976 scans (CN) and 33,888 scans (CNS) for each of the three experiments with different contact times; FIDs processed with 40 Hz (2 ppm) of line broadening. Polarization inversion spectra were acquired with 33,888 scans. A 300-s relaxation delay preceded all ^{15}N experiments. Chemical shifts are relative to ^{15}N-labeled glycine defined as -347.54 ppm (relative to nitromethane at 0 ppm).[2] Additional details are in figure captions.

To validate the presence of chemically bonded acidic sites on the CNS, ammonia temperature programmed desorption (NH_3-TPD) was carried out using Micromeritics AutoChem II 2920. For the measurement, 100∼200 mg of fresh sample was pre-treated with pure He at 120 ℃ for 20 min to remove H_2O that physically adsorbed on the catalyst surface. Then, the adsorption of ammonia was performed using a flow of 50 sccm of 10% NH_3/He (provided by Praxair) for 30 min. After flowing He for 30 min to remove any physically adsorbed NH_3 at 120 ℃, Temperature programmed desorption (TPD) was carried out by ramping to 450 ℃ at 10 ℃/min and a hold of 10 min under He with the rate of 50 sccm. A well calibrated thermal conductivity detector (TCD) determined the amount of desorbed NH_3.

The surface/subsurface (~10 nm) chemical composition of CN and CNS were determined using X-ray photoelectron spectroscopy (XPS) acquired on an Axis-Ultra, Kratos Analytical instrument using a monochromatic Al-Kα source (15 kV, 50 W) with 1486.7 eV photon energy under

ultrahigh vacuum (~10^{-8} Torr). The C1s peak binding energy of adventitious carbons at BE ≈ 284.8 eV was assigned as a standard to calibrate the binding energy of all other elements. The valence band position of the materials was determined using the XPS valence band spectra.

The periodicity and crystalline nature of the CN and CNS samples were determined by using X-ray diffraction (XRD) recorded on a Bruker D8 Discover instrument using Cu-Kα radiation (40 kV, λ = 0.15418 nm) equipped with a LynxEYE 1-dimensional detector. The spectra were accumulated by using a scan size of 0.02° within a 2θ range of 4–60°. The nature of chemical functional groups on the materials and their vibrational features were investigated by using Fourier transform infrared (FT-IR) spectroscopy on a Perkin Elmer Frontier FT-Infrared Spectrophotometer equipped with a ZnSe ATR accessory. For the measurement, the powdered samples were mounted on a ZnSe crystal in an ATR assembly and pressed with a torque knob. The spectra were collected in scans in the frequency range of 400–4000 cm^{-1} and the final spectra were obtained by the accumulation of 32 scans. UV-Vis diffuse reflectance spectra of the solid samples were measured on a Perkin Elmer Lambda-365 UV–Vis spectrophotometer equipped with an integrating sphere accessory and a $BaSO_4$ standard. The change in the molecular polarization and associated scattering frequencies of the materials were determined by Raman spectroscopy acquired on a Thermo Scientific DXR2 Raman Microscope integrated with a 532 nm laser excitation maintained on an incident power of 5 mW cm^{-2}. The thermal stability and degradation pattern of surface functional groups present in the CN and CNS catalysts were determined by thermogravimetric analysis (TGA)-differential scanning calorimetry (DSC) recorded on a thermal analyzer PerkinElmer STA 6000. The measurement was performed in the temperature range of 40–800 °C under nitrogen (30 mL/min) with a heating rate of 5 °C/min.

2.0 Synthesis of materials

2.1 Synthesis of sulfonate/sulfate functionalized carbon nitride (CNS)

The synthesis of sulfonate/sulfate functionalized carbon nitride (CNS) was performed via a solid-state synthesis by thermal condensation polymerization of dicyandiamide and ammonium persulfate in a sealed quartz ampoule. In brief, 500 mg dicyandiamide and a certain amount of ammonium persulfate were thoroughly mixed and charged in a one-sided sealed quartz ampoule. Then the quartz tube was sealed from both sides and heated in a muffle furnace at 550 ºC with a heating rate of 8 °C min^{-1} up to 300 ºC and 2 °C min^{-1} up to 550 ºC and finally holding the temperature at 550 °C for 4 h. Four samples containing 5, 10, 15 and 20 wt% of ammonium persulfate named CNS-5, CNS-10, CNS-15 and CNS-20 were prepared by mixing 25, 50, 75 and 100 mg of ammonium persulfate followed by thermal annealing at 550 °C for 4 h.

Note: *The quartz remains at high pressure during/after synthesis and can explode unexpectedly, thus should be handled carefully using polycarbonate shields and PPE.*

2.2 Synthesis of graphitic carbon nitride, g-C_3N_4, CN [3]

For comparison, we have prepared graphitic carbon nitride. The synthesis of g-C_3N_4 with a nanoporous structure was achieved by using a thermal condensation polymerization of dicyandiamide in a semi-covered system. Briefly, 4 g dicyandiamide crystalline powder was placed in an alumina crucible and coved with a lid. The crucible was subjected to programmed heating at 550 ºC with a rate of 8 °C min^{-1} up to 300 ºC, 2 °C min^{-1} up to 550 ºC and holding at 550 °C for 4 h. A yellow solid obtained was grounded and used for further comparison.

2.3 Synthesis of sulfonated graphitic carbon nitride, S-GCN[4]

For comparison, the sulfonated graphitic carbon nitride was also prepared using previously reported protocol.[4] In brief, 1.0 g of g-C_3N_4 powder was suspended in 50 mL dichloromethane in

a round bottom flask. In the resulting suspension 0.5 mL chlorosulfonic acid was added dropwise for 10 min under continuous stirring and kept for 3 h under stirring conditions. The resulting material was separated by centrifugation and washed with methanol and water and dried under vacuum at 50 °C.

3.0 Hydrothermal dehydration of glucose to levulinic acid

To evaluate the performance of the synthesized catalyst, the conversion of glucose to levulinic acid via dehydration was chosen as a model reaction. A hydrothermal approach at various temperatures was employed for the catalytic reaction. In brief, 10 mg of CNS (CNS-5, CNS-10, CNS-15 and CNS-20) catalysts, and 100 mg of glucose were dispersed in 10 mL DI water and transferred to a Teflon-lined autoclave. The autoclave was heated at three different temperatures c.a. 120, 150 and 200 °C. The autoclave was cooled after 4 h reaction and the obtained mixture was centrifuged to remove the catalysts and humus. The supernatant was filtered through a syringe filter (2 μm PTFE) and diluted 10 times with DI water. The solution was then analyzed/quantified by high-performance liquid chromatography (HPLC; Agilent HPLC) equipped with an HPX-87H column and RID detector and using a 5 mM sulfuric acid as the mobile phase. A calculated amount of standard samples were injected in HPLC and a calibration curve is made for the exact quantification of the sample. Further confirmation of various products was done by using GC-MS and NMR.

The yield of Levulinic acid was calculated as follow:

The yield of LLA (%) = (Moles of LLA obtained/Initial moles of glucose) × 100%

The selectivity of LLA (%) = (Moles of LLA obtained/moles of total product) × 100%

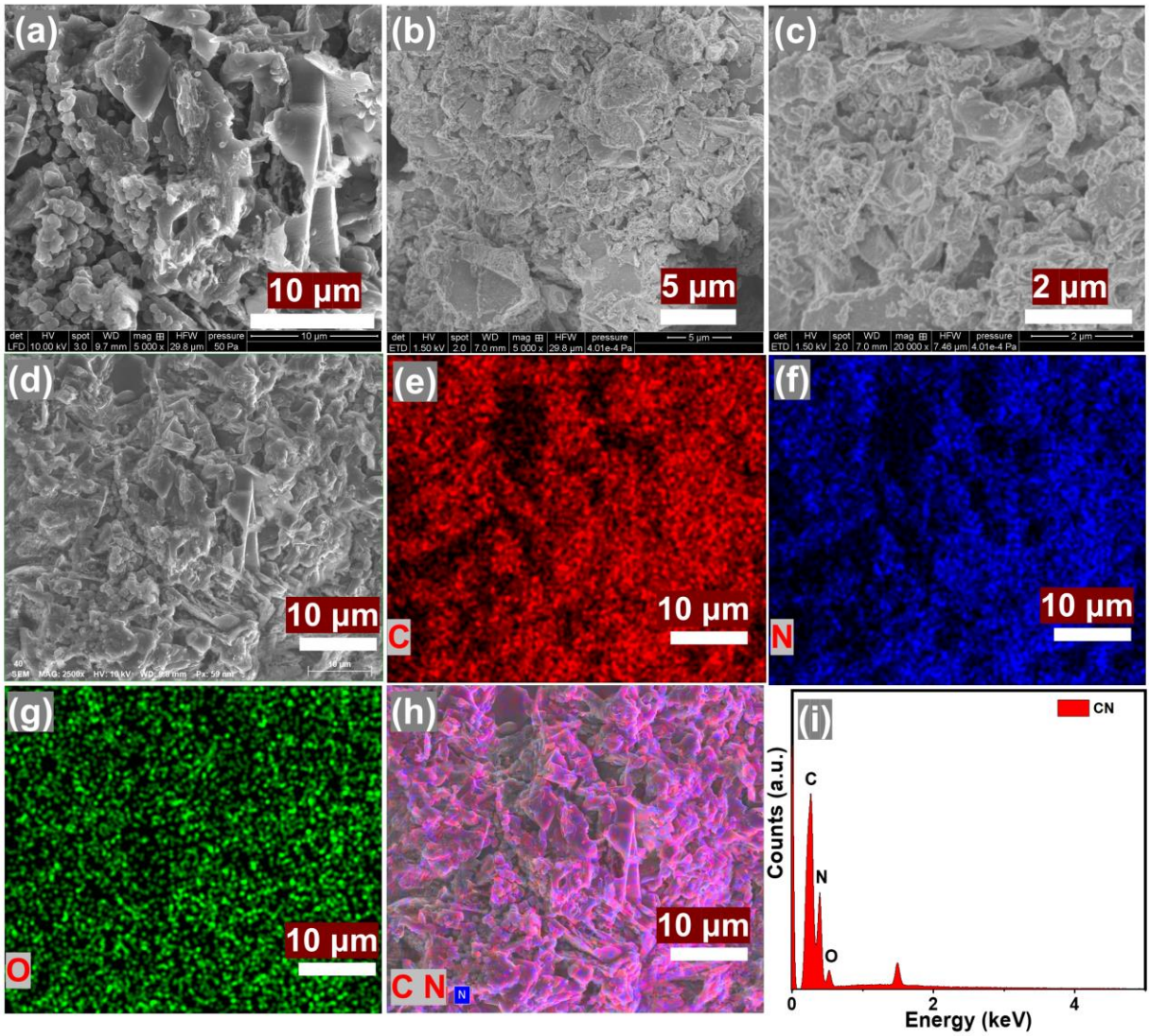

Figure S1. (a-c) FE-SEM image of CN at different magnifications; Elemental mapping of CN (d) electron image showing scanned area and mapping for (e) C: red (f) N: blue (g) O: green (h) O: Composite of C and N, (i) EDX spectra.

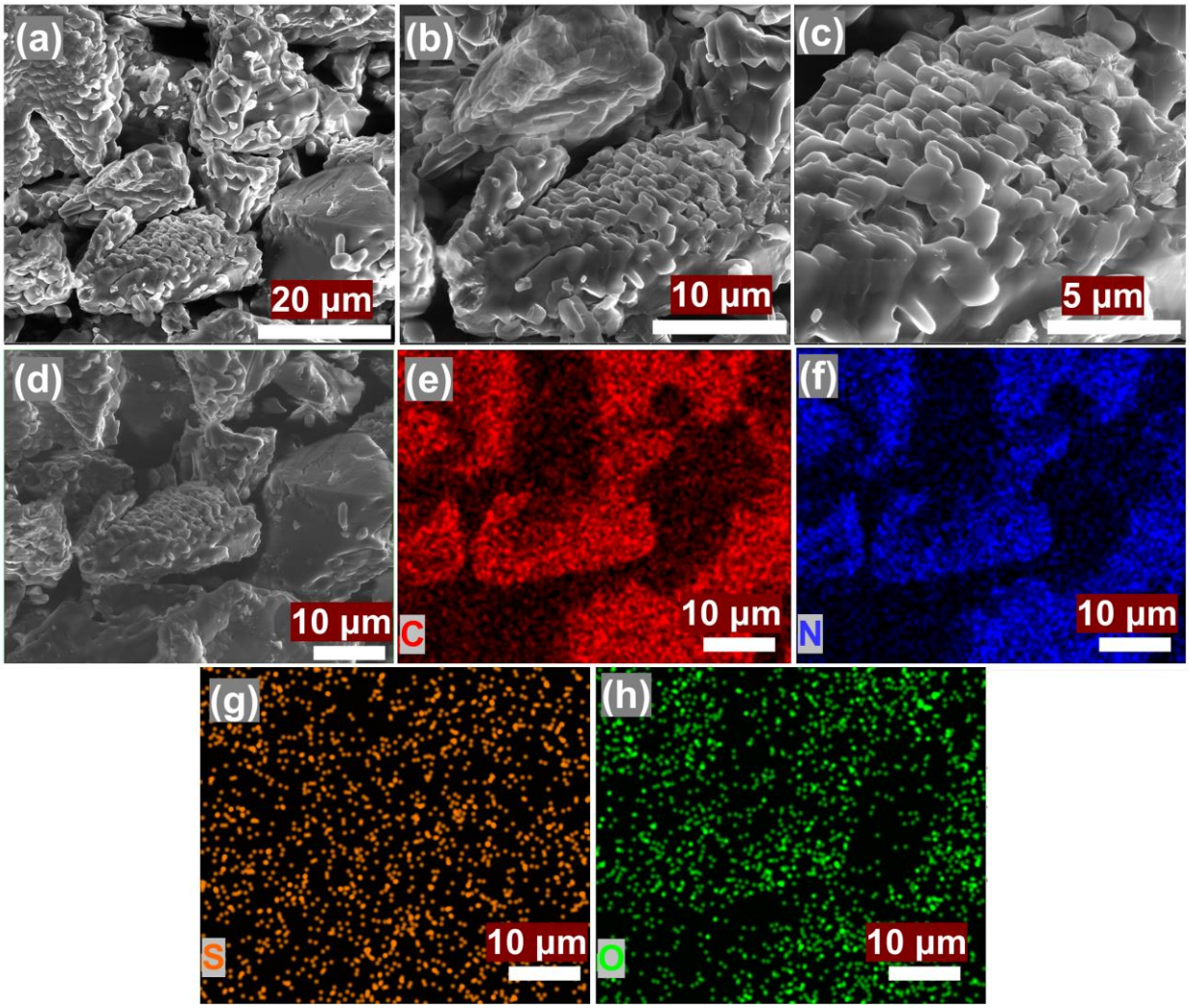

Figure S2. (a-c) FE-SEM image of CNS at different magnifications; Elemental mapping of the CNS (d) electron image showing scanned area and mapping for (e) C; red (f) N; blue (g) S; orange (h) O; green

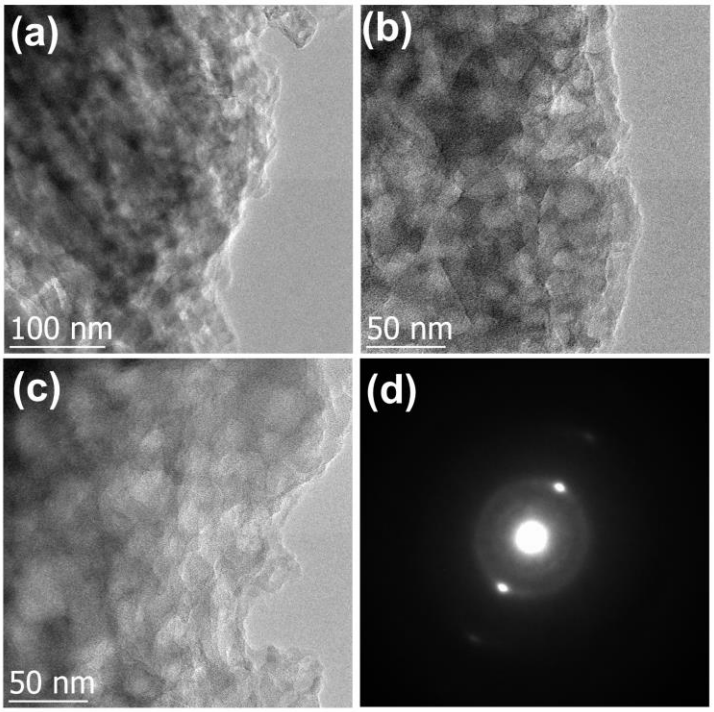

Figure S3. (a-b) HR-TEM images of CNS at different magnification; (c-d) TEM image of CNS showing the porous structure of CNS with the corresponding SAED pattern.

4.0 Additional characterization

4.1 X-ray diffraction

The crystalline nature and periodic structure of the samples were determined by using X-Ray diffraction (**Figure S4**). The XRD spectrum of pristine bulk CN exhibited two signature peaks at 2θ values of 27.4 and ~13.5° ascribed to (002) and (100) planes of the heptazine (C_6N_7) constituted graphitic carbon nitride framework. The XRD diffraction peak at 27.4° with relatively higher intensity was ascribed to interplanar stacking of carbon nitride sheets with a 0.32 nm interplanar *d* spacing.[5, 6] Another less intense XRD signal centered at ~13.5° with 0.68 nm spacing was assigned to the in-plane periodic arrangement of heptazine (C_6N_7) units in the CN network.[7] Furthermore, two weak XRD peaks at ~43.9 and ~56.6° were specific to (300) and (004) reflections of the carbonaceous skeleton. CNS obtained from the solid-state synthesis also exhibited characteristics (002) peaks of the carbon nitride, suggesting that during the synthesis of

CNS the basic carbon nitride framework remains intact. Additionally, some new XRD peaks at 10.6, 11.0, 14.1, 17.5, 21.1, 23.0, 25.5 and 30.1º appeared, which might be because of the S-functionalization in the carbon nitride network.

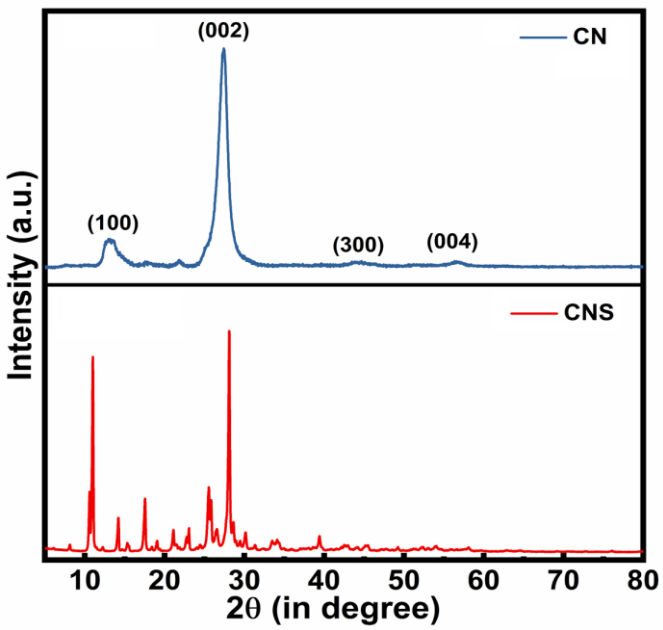

Figure S4. X-ray diffraction spectra of (a) CN and (b) CNS.

4.2 Raman analysis

The Raman active change in the molecular polarization and associated scattering frequencies of CN and CNS were determined using Raman spectroscopy under a 532 nm laser excitation (**Figure 4b**). The Raman spectrum of CN displays a broad intense peak located at 1498 cm^{-1} attributed to combinational vibration of D and G bands of the graphitic carbon nitride structure.[8, 9] The deconvolution of Raman spectra shows two well-resolved D and G bands centered at 1329 and 1644 cm^{-1}.[10] The G band (E_{2g} mode) in graphitic carbon nitride structures originates from the in-plane vibration of the sp^2 bonded C-N structure.[11, 12] The D band originated from the out-of-plane vibration of sp^3 hybridized C-N and represents the defect state. The observance of D band at a relatively lower frequency in CN compared to defect rich graphene/graphene oxide can be

explained due to the presence of more electronegative sp^2 N atoms compared to equally electronegative sp^2 C in graphenic structure.[13] The variable bond angle in carbon nitride due to the presence of alternate sp^2 N atoms linked to sp^2 C, the heptazine-based carbon nitride structure is not completely planer.[14] This non-planer C-N structure facilitates unsynchronized out-of-plane vibration resulting in the appearance of a broad D band. The peak area and intensity of the D band depends on the nitrogen's population in graphenic structure and numbers of functional groups. The CNS samples displayed both D and G bands corroborating the well-constituted carbon nitride framework.[15]

4.3 Dispersibility, Zeta Potential (ζ) and average particle size (*d*.nm)

The dispersibility behavior of the materials was determined by physically suspending the materials in DI water followed by 5 min sonication. It can be seen from **Figures S5a and b** that both CN and CNS were dispersible in water under sonication. However, CN demonstrates significant settlement after 5 min of cessation of sonication (**Figures S5a and b Lower panel**). The increased dispersibility of CNS compared to CN was assumed due to the presence of polar hydrophilic sulfonate/sulfate groups. To probe the hypothesis, we calculated the surface charge distribution on the materials using zeta potential measurement (**Figures S6a and b**). The apparent Zeta Potential (ζ) for the CN and CNS was found to be -29.1 and -38.1 mV demonstrating more surface negative charge on the surface of CNS compared to CN. The ionization of sulfonates and sulfate groups in an aqueous solution renders the CNS surface negatively charge leading to increased dispersibility.

Additionally, the average particles size distribution of CN and CNS was also determined by dynamic light scattering (**Figures S7a and b**) The average diameter of CN and CNS was found to be 1314 and 2480 nm. Paradoxically, the average particles diameter of CNS was much higher than expected which can be explained based on the higher solvation degree of sulfonate/sulfate

functionalized carbon nitride. Due to the high electrostatic charge, more water molecules entourage the CNS sheets than pristine leading to an increased hydrodynamic radius of the CNS.[16, 17]

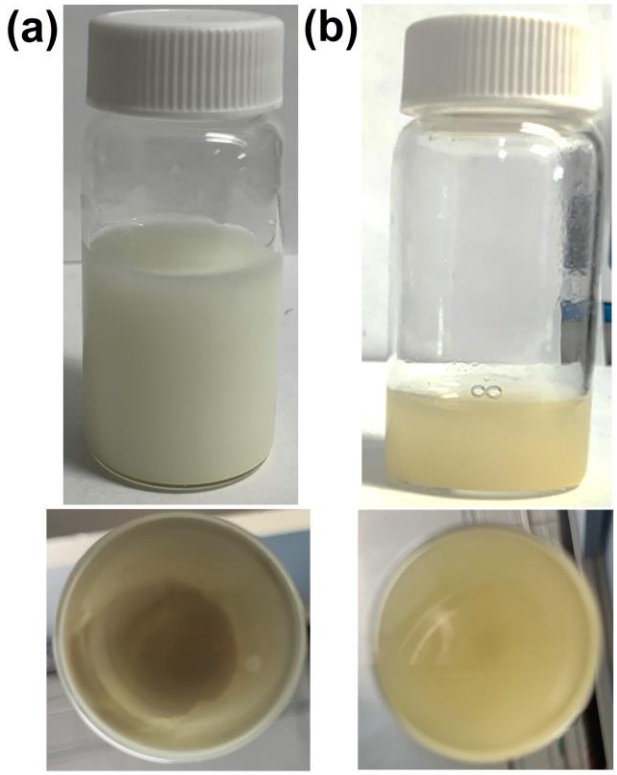

Figure S5. Digital photograph of (a) CN and (b) CNS suspension after 5 min sonication and 5 min rest time. The bottom panel shows the better dispersibility of CNS compared to CN.

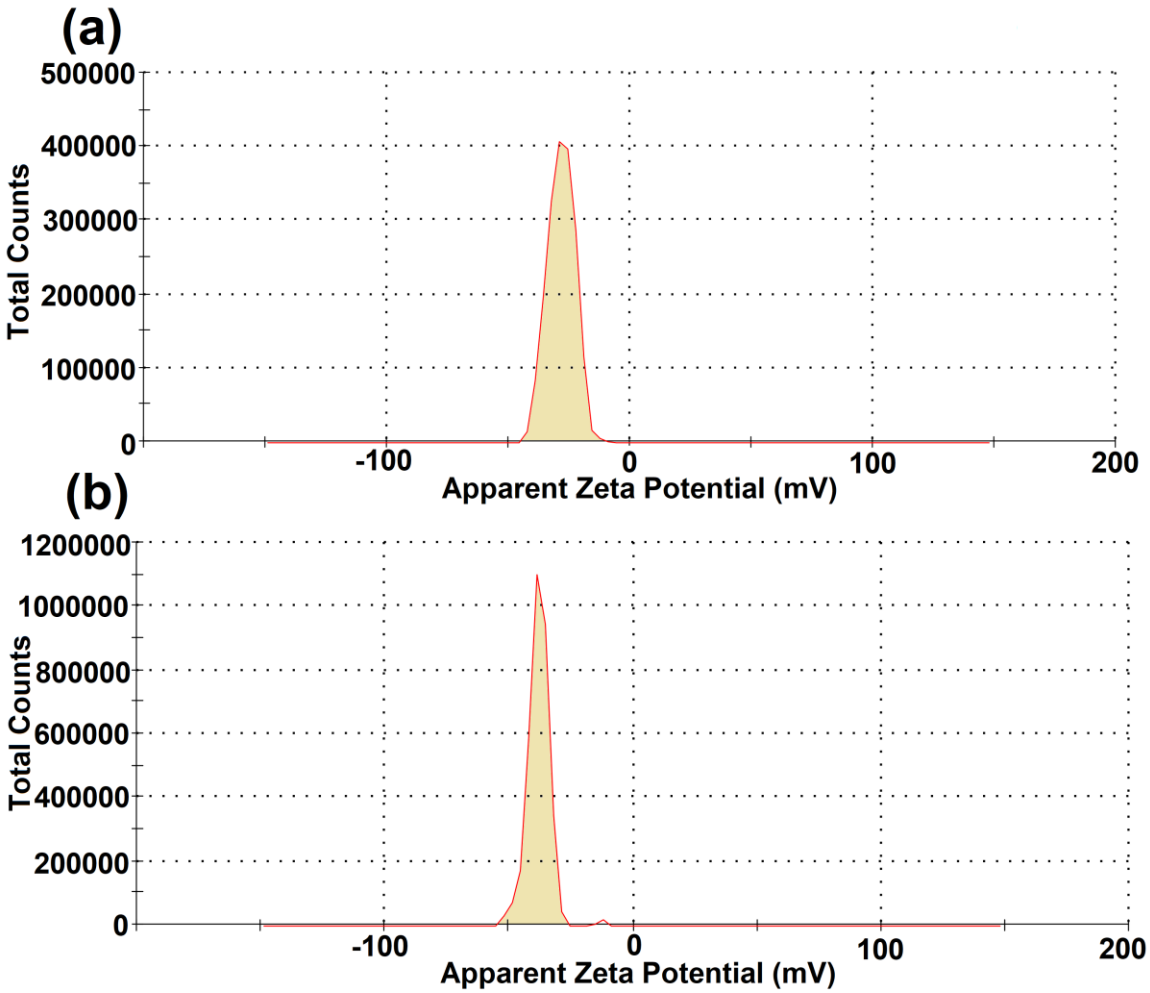

Figure S6. Apparent zeta potential (ζ) of (a) CN (b) CNS.

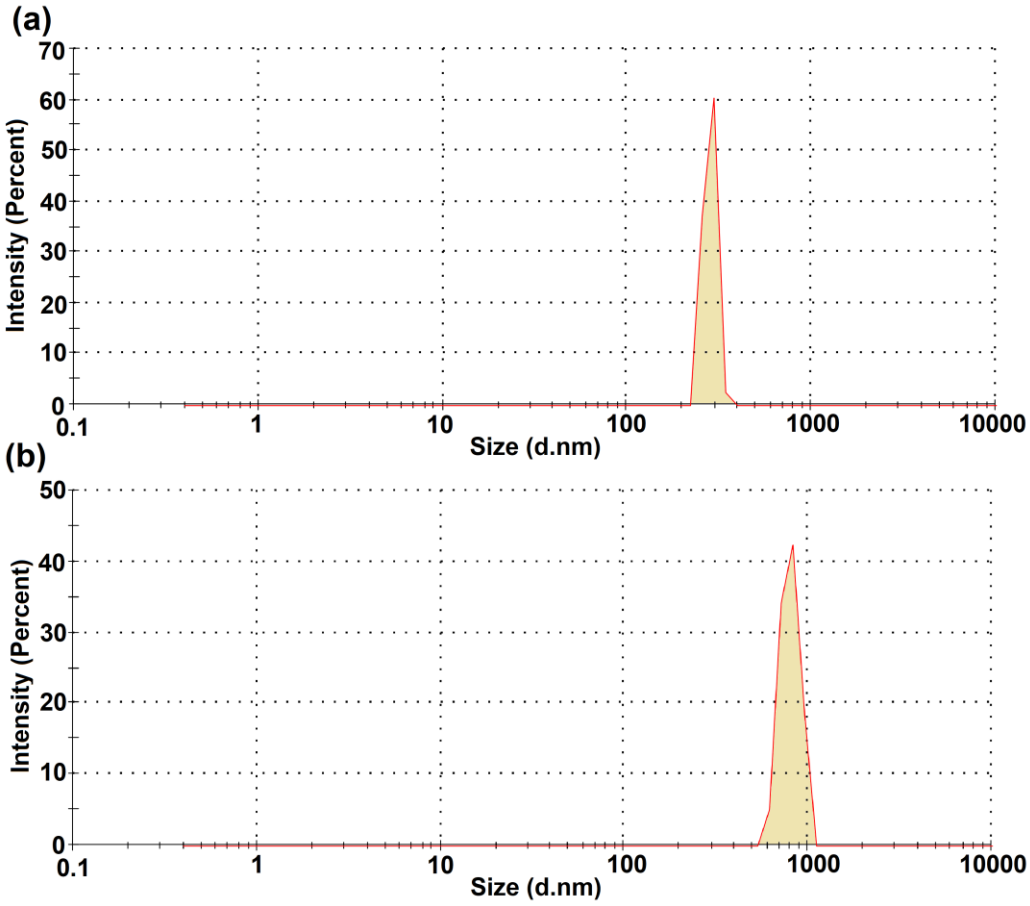

Figure S7. Average particle size distribution of (a) CN and (b) CNS calculated using DLS.

4.4 Thermogravimetric analysis (TGA)-Differential scanning calorimetry (DSC)

The nature of surface chemical functionalities and thermal stability of the samples was determined using thermogravimetric analysis- Differential scanning calorimetry (DSC) TGA-DSC in the temperature range of 45-800 °C under nitrogen. The TGA thermogram of CN displayed a minor weight loss in the temperature range of 50-150 °C attributed to loss of physio-adsorbed water molecules (**Figure S8a Lower panel**). After that CN displayed significant stable behavior up to 500 °C demonstrating well-condensed heptazine motifs in the CN scaffold.[18] The second major weight loss extended from 600 to 700 °C was due to the degradation of due to degradation of

heptazine moieties.[19] Worthy to mention, the gradual weight loss in the temperature range of 500-650 °C was due to the polymerization of uncondensed heptazine units and concomitant ammonia evolution. Furthermore, differential scanning calorimetry (DSC) data exhibits the endothermic nature of the degradation throughout the heating which suggests no phase change occurs which complies with the fully condensed CN structure (**Figure S8a Upper panel**). Since the TGA analysis was performed under nitrogen, the sharp peaks for the oxidation of CN organic motifs were not detected, however, a gradual endothermic slope was observed. An exothermic signal around 750 might be originating due to the transformation of organic carbon to inorganic crystalline (ordered) graphitic carbon. Contrarily, the TGA thermogram of CNS exhibited a sharp weight loss (~12%) between 50-150 °C corroborated to loss of surface adsorbed water and removal of residual persulfate residue (**Figure S8b Lower panel**). As per our observation, the CNS sample displayed weak hygroscopic nature which might be associated with the adsorption of water molecules on sulfonate/sulfate groups. After that, another sharp weight loss was observed in the temperature range of 200-370 °C which might be due to the dissociation of sulfonate/sulfate functionalities.[20, 21] These observations were in accordance with NH_3-TPD results which also show a desorption temperature in this range (**Figure 4c**). Interestingly, compared to sulfonate/sulfate functionalities, the observed weight loss was relatively higher suggesting the removal of ligated C-N functionalities as well. Since ssNMR also indicates the presence of smaller fragments, it is probable that SO_3H/SO_4 ligated moieties degrade as well due to extreme functionalization. Finally, weight loss due to the condensation and degradation of heptazine moieties was observed in the temperature range of 550-700 °C. DSC of CNS also demonstrates similar endothermic attributes assigned to no phase changes and energy-intensive nature of functional group removal substantiating covalent bonding of sulfonate/sulfate groups (**Figure S8b Upper panel**). Though,

the thermal feature was endothermic, a slight exothermic feature around 150 °C might be due to the removal of surface adsorbed sulfur-containing groups.

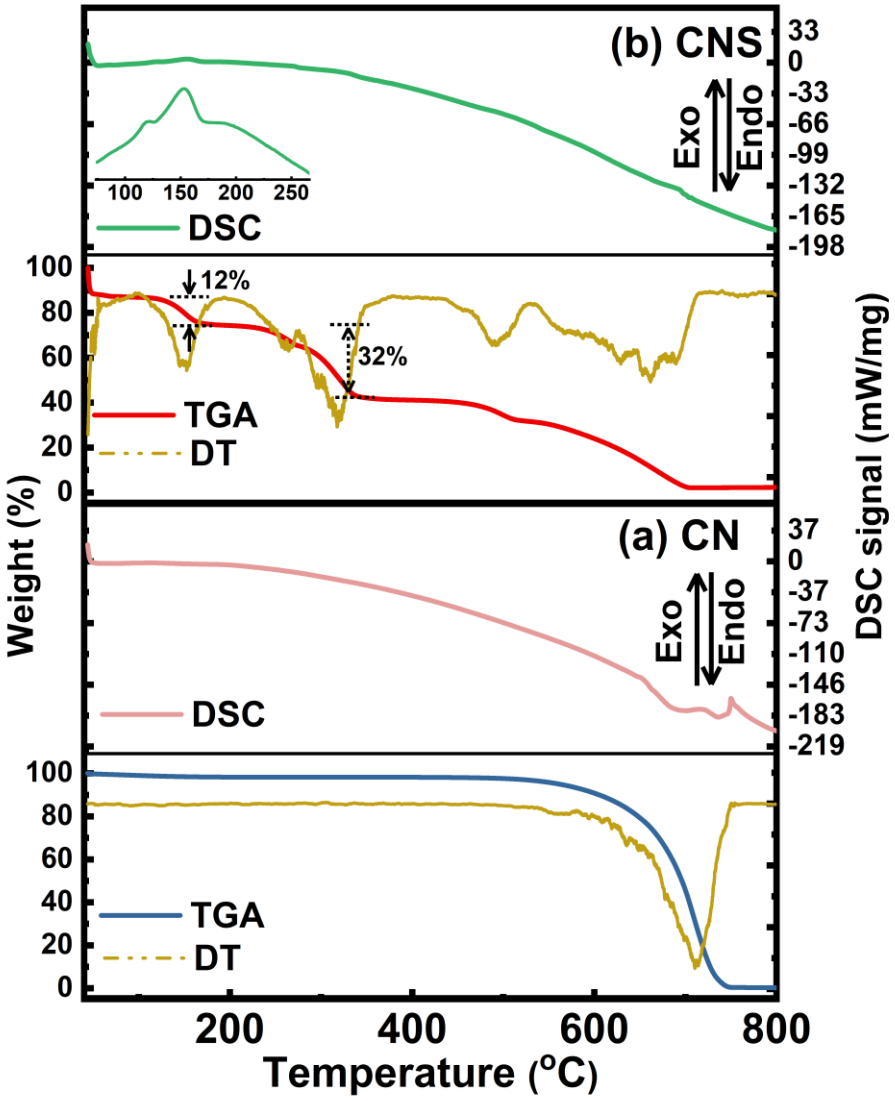

Figure S8. (a) Lower panel: TGA and DTA of CN Upper panel: DSC thermogram of CN (b) Lower panel: TGA and DTA of CNS Upper panel: DSC thermogram of CNS. Arrows showing exothermic and endothermic direction of the signals.

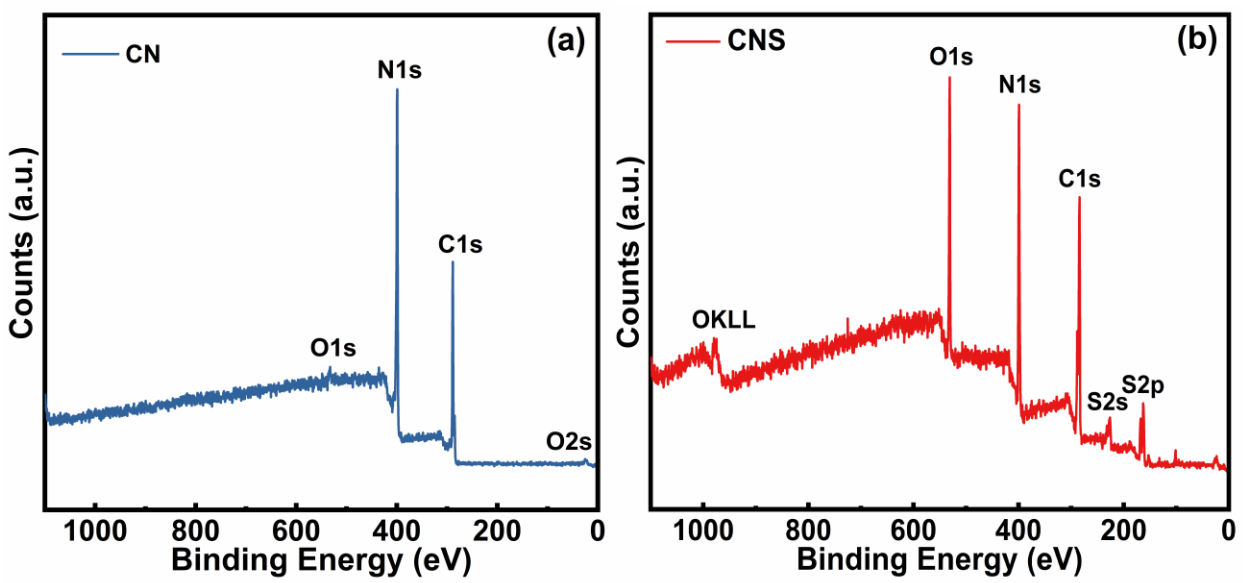

Figure S9. XPS elemental survey scan of (a) CN and (b) CNS.

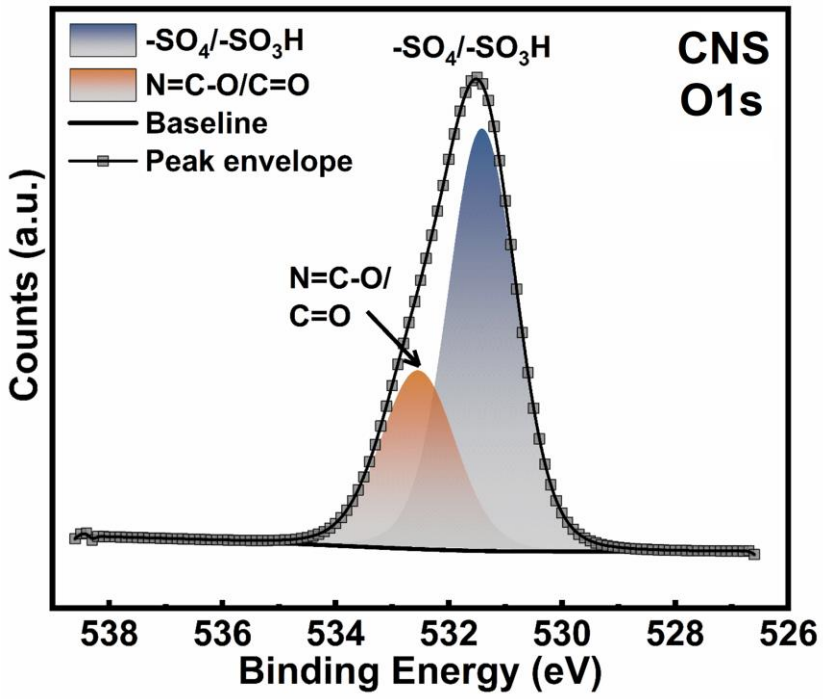

Figure S10. HR-XPS spectra of CNS in O1s region

5.0 UV-Vis and XPS valence band spectra

The electronic absorption of the materials was determined by using UV-vis spectra collected in diffuse reflectance mode. The UV-Vis spectrum of CN displayed a narrow band at the 300 nm and another wide intense band extending in the range of 355-400 nm ascribed to $\pi \rightarrow \pi^*$ transition and $n \rightarrow \pi^*$ transition in carbon nitride framework.[22] The broad CN band in the region between 300-440 nm with an extended absorption tail was originated from the direct band to band transition from N 2p constituted valence band to the C 2p constituted conduction band.[23] After the S doping and sulfonate/sulfate functionalization the absorption profile of the materials was enhanced all the way up to the NIR region demonstrating the decreased bandgap due to the participation of S lone pairs in the π-conjugated carbon nitride framework. Previous studies suggest that doping of S atom in CN network proceeds via the replacement of C atom which provides sub energy levels and resulting in uplifting of the valence band.[24, 25] To verify this hypothesis, we have collected XPS valence band spectra of the CN and CNS samples. The XPS valence band spectra of CN show the valence band maxima (VBM) at 1.87 eV below the Fermi level while VBM for the CNS was found at 1.10 eV corroborating the uplifting of VBM after the functionalization.

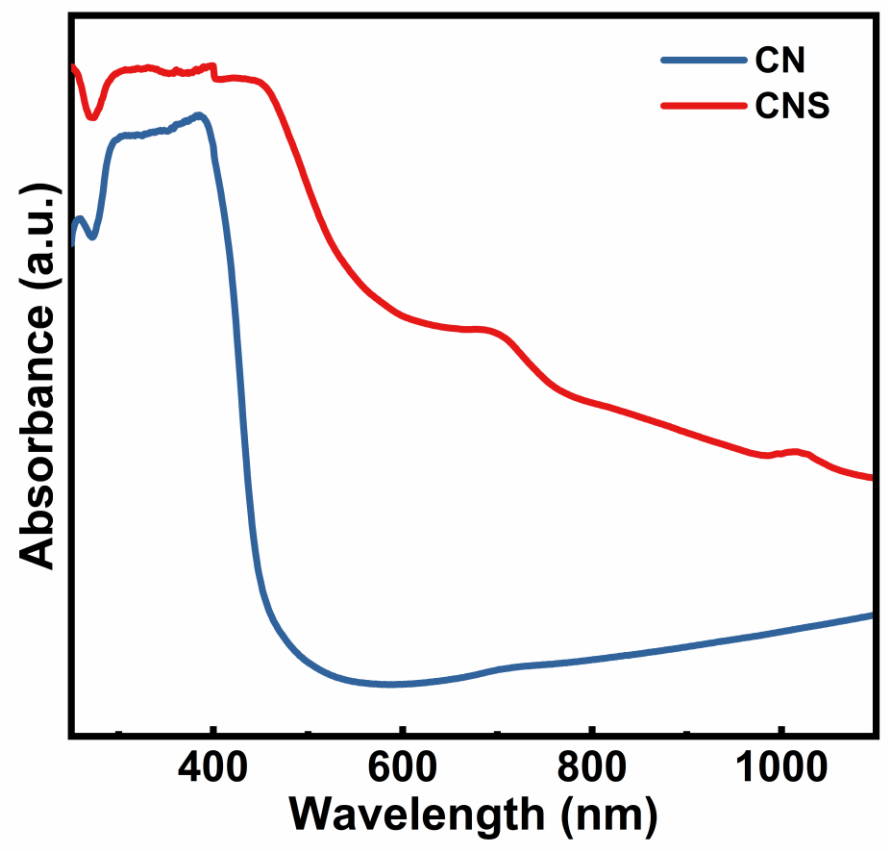

Figure S11. UV-Vis DRS spectra of CN and CNS.

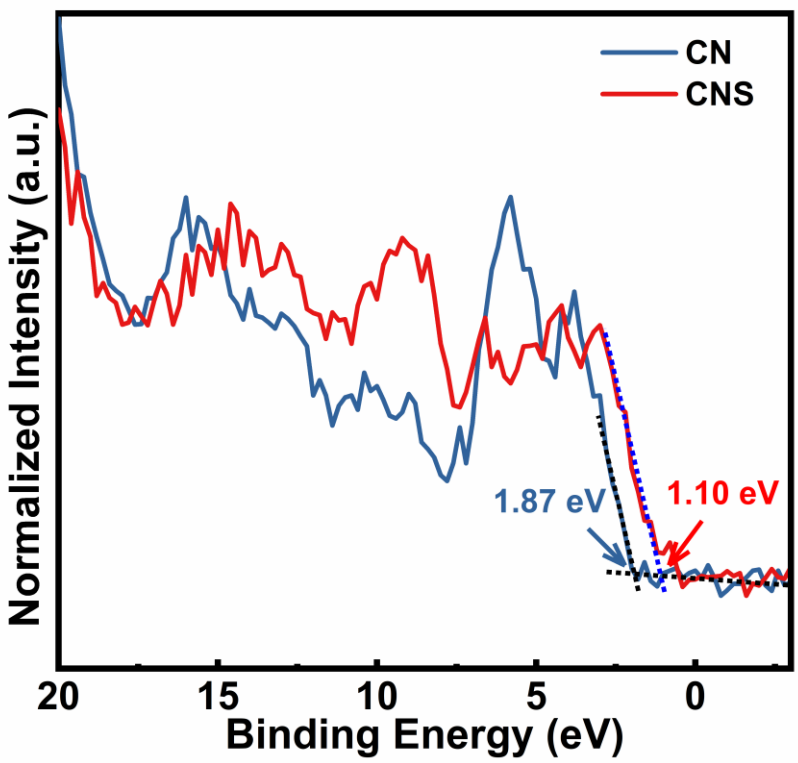

Figure S12. XPS valence band (VB) spectra of CN and CNS.

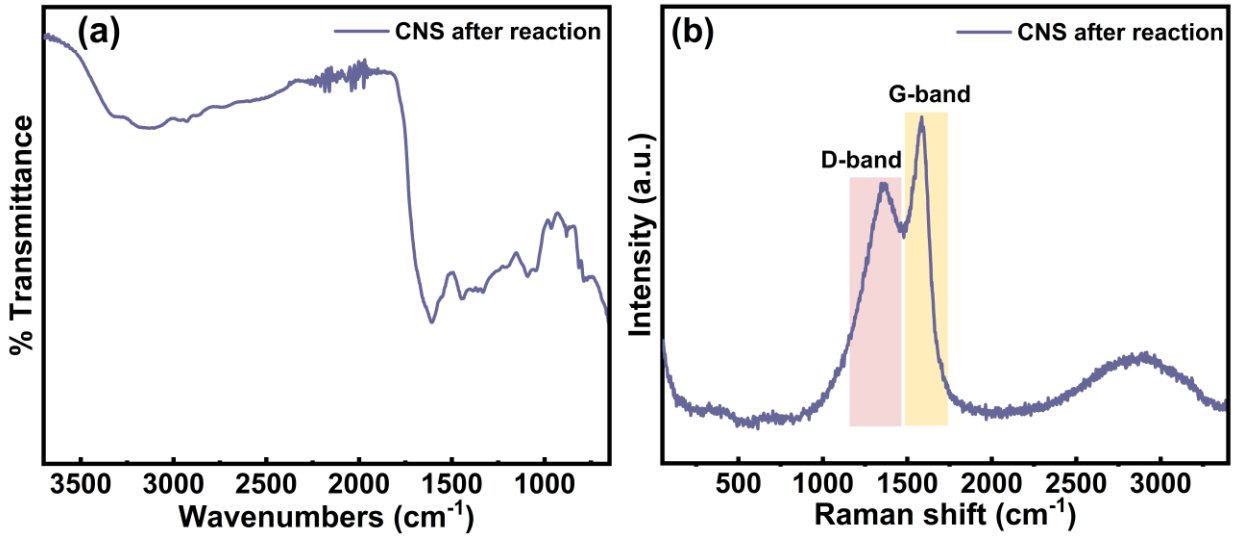

Figure S13. (a) FTIR spectra of recycled CNS catalysts after reaction and washing with THF (b) Raman spectra of recycled CNS catalysts after reaction and washing with THF.

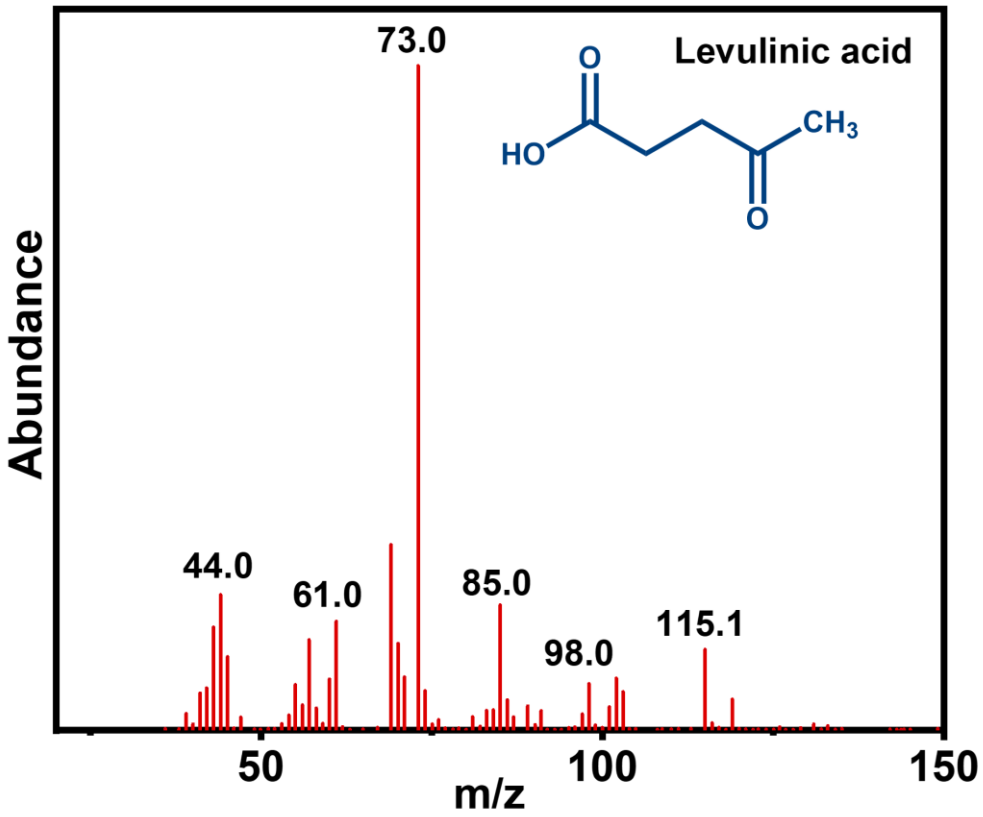

Figure S14. GC-MS spectra of glucose hydrothermal conversion products using CNS showing levulinic acid fragmentation pattern peaks.

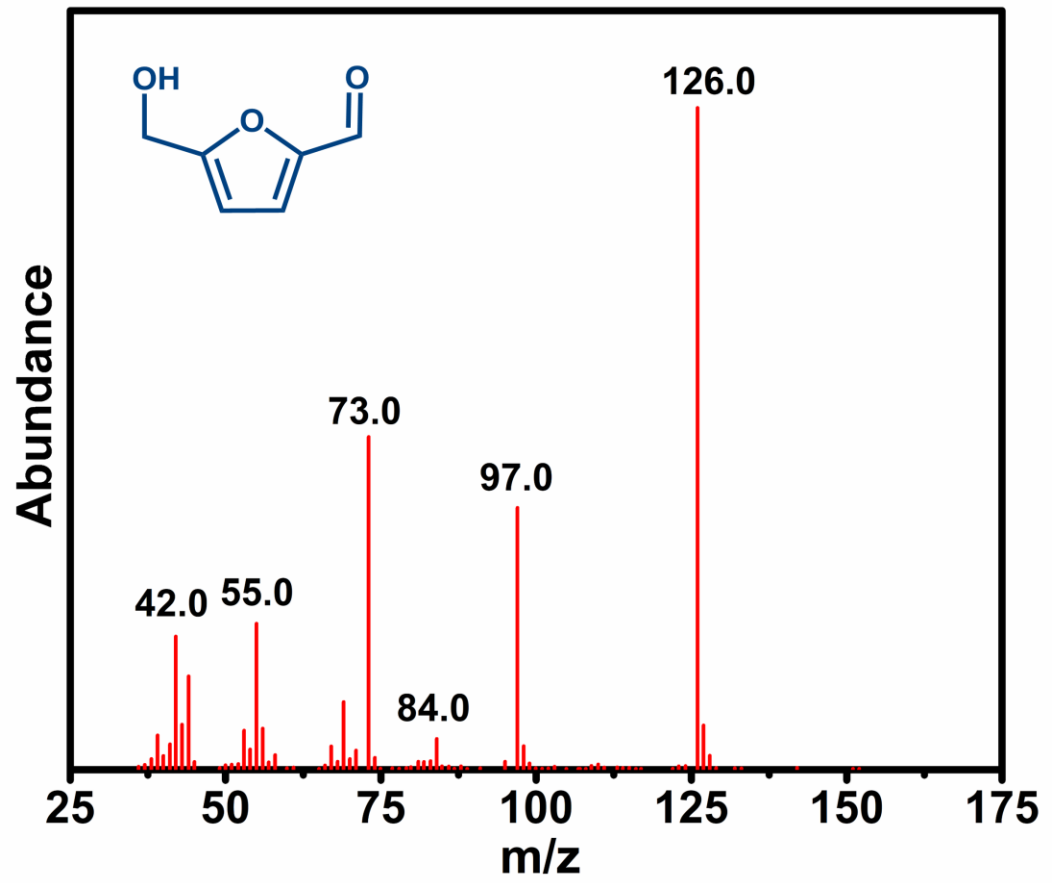

Figure S15. GC-MS spectra of glucose hydrothermal conversion products using CNS showing HMF fragmentation pattern peaks.

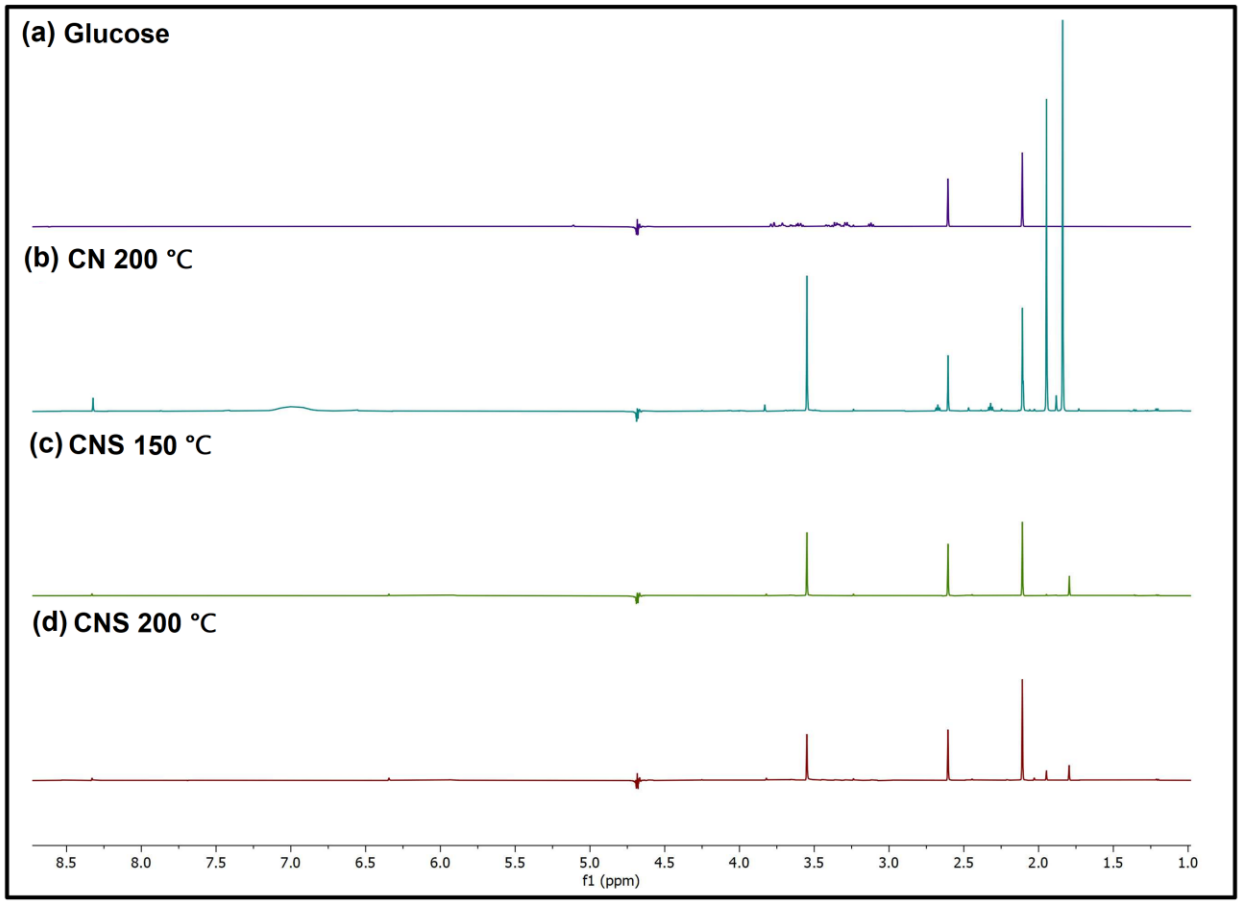

Figure S16. Overlayed ^{1}H NMR spectra of (a) glucose, after hydrothermal treatment of glucose (b) at 200 ℃ using CN, (c) at 150 and (d) 200 ℃ using CNS.

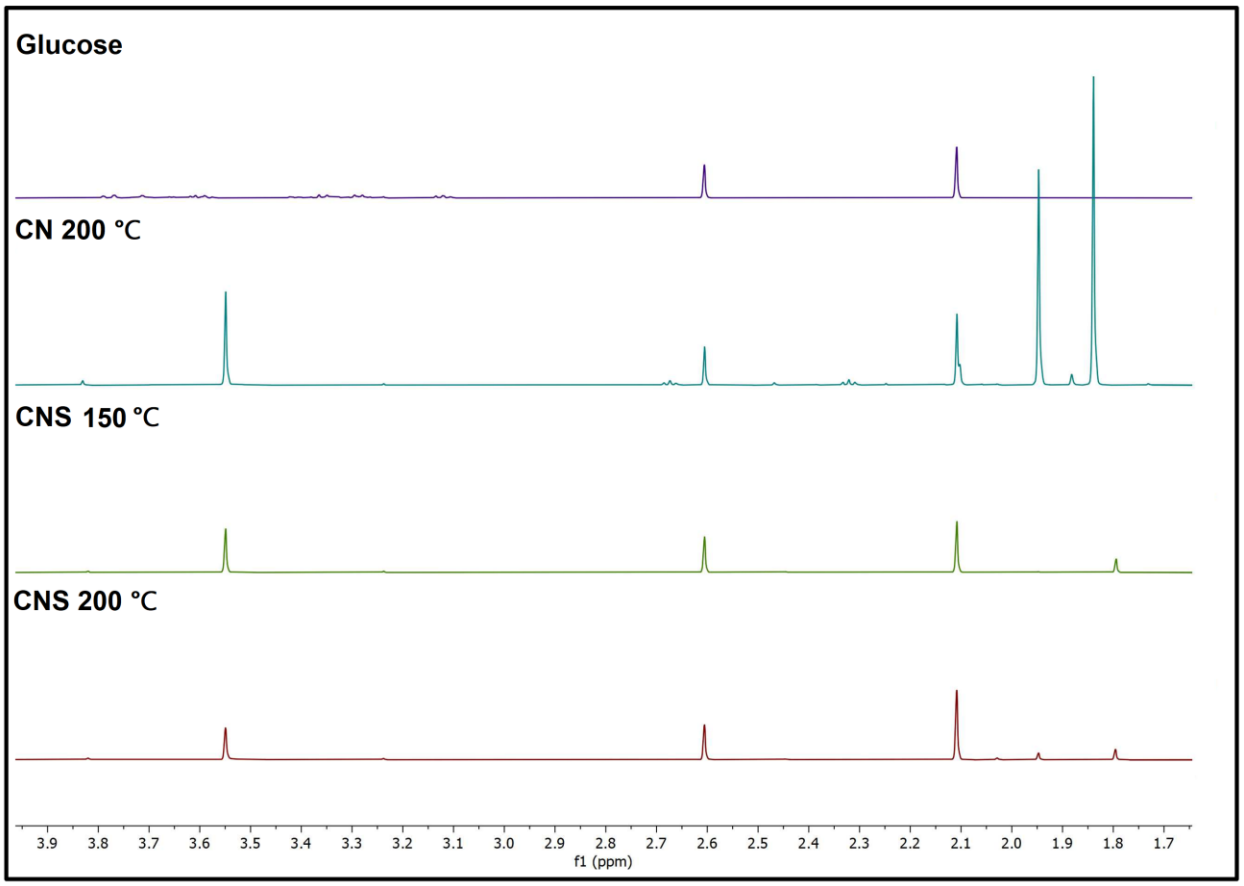

Figure S17. Expanded overlayed ^{1}H NMR spectra of (a) glucose (δ 1.7-3.9 ppm), after hydrothermal treatment of glucose (b) at 200 °C using CN, (c) at 150 and (d) 200 °C using CNS.

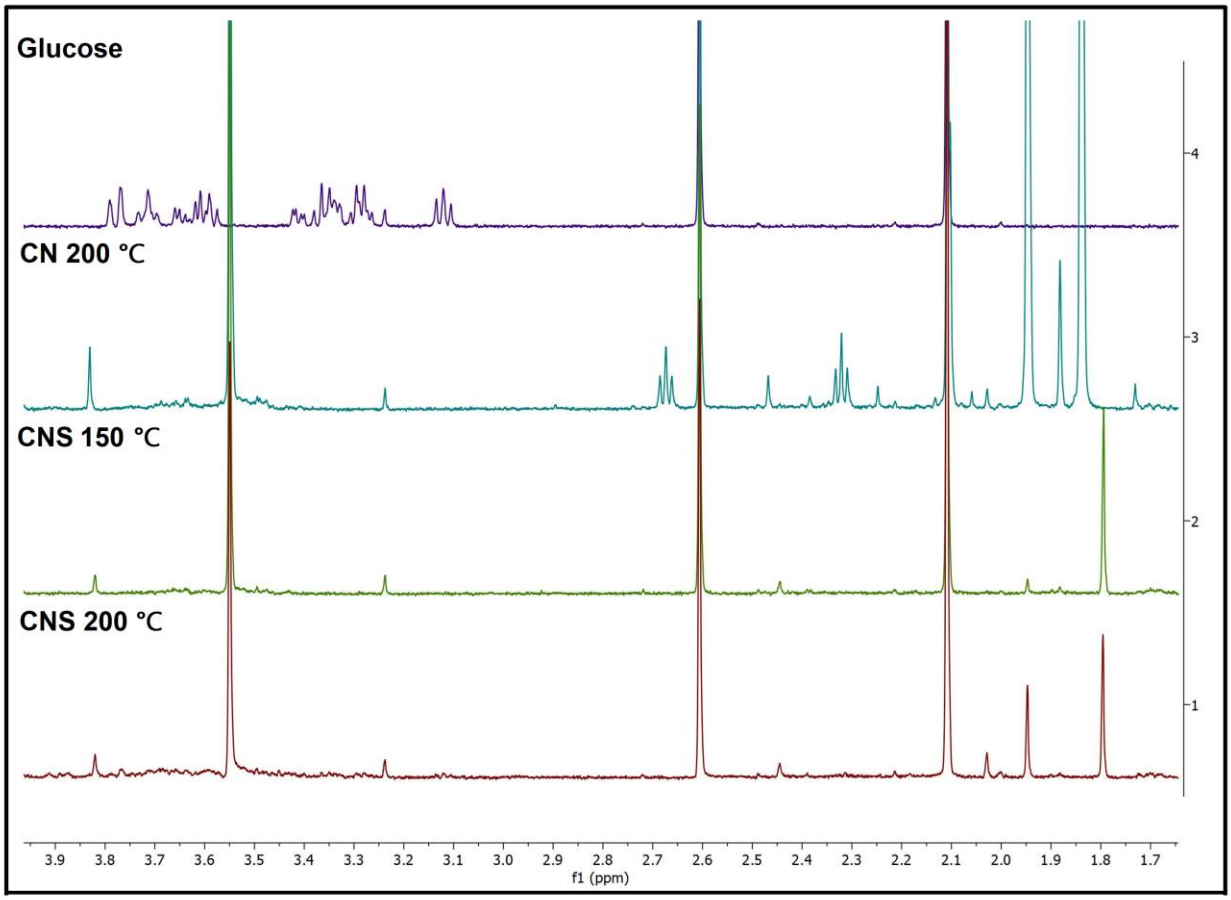

Figure S18. Zoomed overlayed ^{1}H NMR spectra of (a) glucose (δ 1.7-3.9 ppm), after hydrothermal treatment of glucose (b) at 200 °C using CN, (c) at 150 and (d) 200 °C using CNS.

Table S1. The yield of various products obtained from the hydrothermal treatment of glucose using CN and CNS as catalysts at 120 ℃, 150 ℃ and 200 ℃

Product	CNS (120 ℃)	CNS (150 ℃)	CNS (200 ℃)	CN (200 ℃)
Levulinic acid	28.0	36.0	47.9	20.0
Formic acid	7.0	8.1	10.5	5.54
Erythrose	28.0	16.5	11.6	8.18
Acetic acid	28.0	19.0	14.0	60.42
Lactic acid	4.3	4.8	4.9	1.27
Glycolic acid	-	-	-	2.12
HMF	-	-	-	1.74

Reaction conditions: glucose: 0.1 g, catalyst: 10 mg, DI water: 10 mL for 4 h.

Table S2. Catalytic performance of S-GCN and CNS toward the conversion of glucose and fructose.

	Glucose	Fructose
Product	**SGCN (200 ºC)**	**CNS (200 ºC)**
Levulinic acid	0.00	35.05
Formic acid	10.36	4.91
Erythrose	0.00	18.63
Acetic acid	14.03	22.60
Lactic acid	8.94	0.45
Glycolic acid	0.00	3.76
HMF	52.22	9.53

Table S3. Comparison of glucose to levulinic acid conversion using variously reported catalysts

No.	Catalysts	Temperature (℃)	Solvent	Yield (%)	Remarks	Ref.
1	$C_6H_{15}O_2N_2)_{3-x}H_xPW_{12}O_{40}$ (abbreviated as $Ly_{3-x}H_xPW$	140	Choline chloride soluti on	52.6%	Use expensive elements for catalyst and choline chloride	[26]
2	a-SA and a-SAPO	180	DI water	40	Tedious catalyst synthesis in the glove box and expensive precursors and Ar pressurized at 20 bar	[27]
3	$CrCl_3$ (10 w/v%) with HY zeolite powder	160	Water	63	Toxic chromium and tedious catalysts synthesis	[28]
4	$-SO_3H$ functionalized Ionic liquid (IL-SO_3H)	155	Water	46.60	Expensive and separation of IL-SO_3H requires organic solvent and reduced drying	[29]
5	Fe/HY Zeolite	180	Water	60	Less robust catalyst. Iron might diffuse to reaction mixture due to wet impregnation synthesis.	[30]
6	SO_4^{2-}/ZrO_2	160	NaCl–THF/H_2O biphasic solvent system	29.60	Uses sulfuric acid for $-SO_3H$ functionalization which	[31]
7	Acidic Ion Exchange Catalyst DOWEX DR-2030	145	Water+Salt	70.7	Needs to regenerate the catalyst	[32]
8	Cr/HZSM-5	180	Water	53.7	Toxic chemicals	[33]
9	H_3PO_4-$CrCl_3$ catalysts	170	Water	54.27	Used acids and toxic Chromium, non-recyclable	[34]
10	IL with $NiSO_4.6H_2O$	175	IL (400 mg catalyst and 600 µL water) and 1.8 wt% metal salts	56.37	Expensive, separation, non-recyclable.	[35]
11	$LiCl{\cdot}3H_2O$	170	Neat	33.92	Expensive and toxic to central nervous system, non-recyclable	[36]
12	Methanesulfonic acid (MSA)	181	Water	48.95	Homogenous, requires stoichiometric catalyst, long reaction time	[37]

14	Ga@HPMo and GaHPMo	175	Water	56 and 46	Expensive Ga and Mo precursors, Tedious synthesis using glovebox and solvent evaporation	[38]
15	Sulfonated graphene oxide (GO-SO_3H)	200	Water	84	Plenty of harsh chemical for the synthesis of GO, use of toxic $ClSO_3H$, less fucntionalization	[39]
16	Fe/HY zeolite	180	Water	64	Non-resilient catalyst. Secondary contamination from leaching.	[40]
17	(Al-$(MA)_2$-$(OH)_2$)	160	Water	30	Using Maleic acid, $AlCl_3$ is reactive to water, non-recyclable	[41]
18	Chromium modified niobium phosphate (Cr/NbP)	180	Water	62	Toxic chromium and expensive niobium	[42]
19	Silicotungstate ($Al_4/_3SiW_{12}O_{40}$)	180	Water	50.4	Deactivate after few runs	[43]
20	Mesoporous niobium-containing oxides (Fe-NbP)	180	Water	64.2	Use toxic HF and ammonia for the synthesis, expensive niobium	[44]
21	**Sulfonate/sulfate functionalized carbon nitride (CNS)**	200	Water	48.6	Synthesized from earth-abundant materials and easy to upgrade at the commercial scale	**This Study**

References

1. Alemany, L. B.; Verma, M.; Billups, W.; Wellington, S. L.; Shammai, M., Solid-and Solution-State Nuclear Magnetic Resonance Analyses of Ecuadorian Asphaltenes: Quantitative Solid-State Aromaticity Determination Supporting the "Island" Structural Model. Aliphatic Structural Information from Solution-State $^{1}H–^{13}C$ Heteronuclear Single-Quantum Coherence Experiments. *Energy Fuels* **2015,** *29* (10), 6317-6329. DOI: https://doi.org/10.1021/acs.energyfuels.5b01455
2. Hayashi, S.; Hayamizu, K., Chemical shift standards in high-resolution solid-state NMR (2) ^{15}N nuclei. *Bull. Chem. Soc. Japan* **1991,** *64* (2), 688-690. DOI: https://doi.org/10.1246/bcsj.64.688
3. Yan, S.; Li, Z.; Zou, Z., Photodegradation performance of g-C_3N_4 fabricated by directly heating melamine. *Langmuir* **2009,** *25* (17), 10397-10401. DOI: https://doi.org/10.1021/la900923z
4. Baig, R. N.; Verma, S.; Nadagouda, M. N.; Varma, R., Room temperature synthesis of biodiesel using sulfonated graphitic carbon nitride. *Sci. Rep.* **2016,** *6* (1), 39387. DOI: https://doi.org/10.1038/srep39387
5. Park, H. L.; Kim, H.; Lim, D.; Zhou, H.; Kim, Y. H.; Lee, Y.; Park, S.; Lee, T. W., Retina-inspired carbon nitride-based photonic synapses for selective detection of UV light. *Adv. Mater.* **2020,** *32* (11), 1906899. DOI: https://doi.org/10.1002/adma.201906899

6. Rahman, M. Z.; Tapping, P. C.; Kee, T. W.; Smernik, R.; Spooner, N.; Moffatt, J.; Tang, Y.; Davey, K.; Qiao, S. Z., A benchmark quantum yield for water photoreduction on amorphous carbon nitride. *Adv. Funct. Mater.* **2017,** *27* (39), 1702384. DOI: https://doi.org/10.1002/adfm.201702384
7. Tian, H.; Liu, M.; Zheng, W., Constructing 2D graphitic carbon nitride nanosheets/layered MoS_2/graphene ternary nanojunction with enhanced photocatalytic activity. *Appl. Catal. B* **2018,** *225*, 468-476. DOI: https://doi.org/10.1016/j.apcatb.2017.12.019
8. Alam, K. M.; Kumar, P.; Kar, P.; Thakur, U. K.; Zeng, S.; Cui, K.; Shankar, K., Enhanced charge separation in gC_3N_4–BiOI heterostructures for visible light driven photoelectrochemical water splitting. *Nanoscale Adv.* **2019,** *1* (4), 1460-1471. DOI: https://doi.org/10.1039/C8NA00264A
9. Liu, B.; Ye, L.; Wang, R.; Yang, J.; Zhang, Y.; Guan, R.; Tian, L.; Chen, X., Phosphorus-doped graphitic carbon nitride nanotubes with amino-rich surface for efficient CO_2 capture, enhanced photocatalytic activity, and product selectivity. *ACS Appl. Mater. Interfaces* **2018,** *10* (4), 4001-4009. DOI: https://doi.org/10.1021/acsami.7b17503
10. Liu, J.; Zhang, Y.; Zhang, L.; Xie, F.; Vasileff, A.; Qiao, S. Z., Graphitic carbon nitride (g-C_3N_4)-derived N-rich graphene with tuneable interlayer distance as a high-rate anode for sodium-ion batteries. *Adv. Mater.* **2019,** *31* (24), 1901261. DOI: https://doi.org/10.1002/adma.201901261
11. Rodil, S.; Ferrari, A.; Robertson, J.; Milne, W., Raman and infrared modes of hydrogenated amorphous carbon nitride. *J. Appl. Phys.* **2001,** *89* (10), 5425-5430. DOI: https://doi.org/10.1063/1.1365076
12. Song, X.; Li, X.; Zhang, X.; Wu, Y.; Ma, C.; Huo, P.; Yan, Y., Fabricating C and O co-doped carbon nitride with intramolecular donor-acceptor systems for efficient photoreduction of CO_2 to CO. *Appl. Catal. B* **2020,** *268*, 118736. DOI: https://doi.org/10.1016/j.apcatb.2020.118736
13. Chowdhury, A.; Cameron, D. C.; Hashmi, M., Vibrational properties of carbon nitride films by Raman spectroscopy. *Thin Solid Films* **1998,** *332* (1-2), 62-68. DOI: https://doi.org/10.1016/S0040-6090(98)00984-5
14. Suter, T.; Brázdová, V.; McColl, K.; Miller, T. S.; Nagashima, H.; Salvadori, E.; Sella, A.; Howard, C. A.; Kay, C. W.; Corà, F., Synthesis, structure and electronic properties of graphitic carbon nitride films. *J. Phys. Chem. C* **2018,** *122* (44), 25183-25194. DOI: https://doi.org/10.1021/acs.jpcc.8b07972
15. Kaufman, J.; Metin, S.; Saperstein, D., Symmetry breaking in nitrogen-doped amorphous carbon: Infrared observation of the Raman-active G and D bands. *Phys. Rev. B* **1989,** *39* (18), 13053. DOI: https://doi.org/10.1103/PhysRevB.39.13053
16. Ma, H.; Bolster, C.; Johnson, W. P.; Li, K.; Pazmino, E.; Camacho, K. M.; Anselmo, A. C.; Mitragotri, S., Coupled influences of particle shape, surface property and flow hydrodynamics on rod-shaped colloid transport in porous media. *J. Colloid Interface Sci.* **2020,** *577*, 471-480. DOI: https://doi.org/10.1016/j.jcis.2020.05.022
17. Hossain, M. I.; Blanchard, G., The effect of dilution on induced free charge density gradients in room temperature ionic liquids. *Phys. Chem. Chem. Phys.* **2022,** 24, 3844-3853. DOI: https://doi.org/10.1039/D1CP05027C
18. Kumar, P.; Vahidzadeh, E.; Thakur, U. K.; Kar, P.; Alam, K. M.; Goswami, A.; Mahdi, N.; Cui, K.; Bernard, G. M.; Michaelis, V. K., C_3N_5: A low bandgap semiconductor containing an azo-linked carbon nitride framework for photocatalytic, photovoltaic and adsorbent applications. *J. Am. Chem. Soc.* **2019,** *141* (13), 5415-5436. DOI: https://doi.org/10.1021/jacs.9b00144

19. Zhao, Y.; Liu, Z.; Chu, W.; Song, L.; Zhang, Z.; Yu, D.; Tian, Y.; Xie, S.; Sun, L., Large-scale synthesis of nitrogen-rich carbon nitride microfibers by using graphitic carbon nitride as precursor. *Adv. Mater.* **2008,** *20* (9), 1777-1781. DOI: https://doi.org/10.1002/adma.200702230
20. Tao, M.-L.; Guan, H.-Y.; Wang, X.-H.; Liu, Y.-C.; Louh, R.-F., Fabrication of sulfonated carbon catalyst from biomass waste and its use for glycerol esterification. *Fuel Process. Technol.* **2015,** *138*, 355-360. DOI: https://doi.org/10.1016/j.fuproc.2015.06.021
21. Younker, J. M.; Saito, T.; Hunt, M. A.; Naskar, A. K.; Beste, A., Pyrolysis pathways of sulfonated polyethylene, an alternative carbon fiber precursor. *J. Am. Chem. Soc.* **2013,** *135* (16), 6130-6141. DOI: https://doi.org/10.1021/ja3121845
22. Kumar, P.; Bansiwal, A.; Labhsetwar, N.; Jain, S. L., Visible light assisted photocatalytic reduction of CO_2 using a graphene oxide supported heteroleptic ruthenium complex. *Green Chem.* **2015,** *17* (3), 1605-1609. DOI: https://doi.org/10.1039/C4GC01400F
23. Lei, G.; Zhao, W.; Shen, L.; Liang, S.; Au, C.; Jiang, L., Isolated iron sites embedded in graphitic carbon nitride (g-C_3N_4) for efficient oxidative desulfurization. *Appl. Catal. B* **2020,** *267*, 118663. DOI: https://doi.org/10.1016/j.apcatb.2020.118663
24. Jourshabani, M.; Shariatinia, Z.; Badiei, A., Controllable synthesis of mesoporous sulfur-doped carbon nitride materials for enhanced visible light photocatalytic degradation. *Langmuir* **2017,** *33* (28), 7062-7078. DOI: https://doi.org/10.1021/acs.langmuir.7b01767
25. Wang, H.; Bian, Y.; Hu, J.; Dai, L., Highly crystalline sulfur-doped carbon nitride as photocatalyst for efficient visible-light hydrogen generation. *Appl. Catal. B* **2018,** *238*, 592-598. DOI: https://doi.org/10.1016/j.apcatb.2018.07.023
26. Sun, Z.; Wang, S.; Wang, X.; Jiang, Z., Lysine functional heteropolyacid nanospheres as bifunctional acid–base catalysts for cascade conversion of glucose to levulinic acid. *Fuel* **2016,** *164*, 262-266. DOI: https://doi.org/10.1016/j.fuel.2015.10.014
27. Beh, G. K.; Wang, C. T.; Kim, K.; Qu, J.; Cairney, J.; Ng, Y. H.; An, A. K.; Ryoo, R.; Urakawa, A.; Teoh, W. Y., Flame-made amorphous solid acids with tunable acidity for the aqueous conversion of glucose to levulinic acid. *Green Chem.* **2020,** *22* (3), 688-698. DOI: https://doi.org/10.1039/C9GC02567G
28. Ya'aini, N.; Amin, N. A. S.; Endud, S., Characterization and performance of hybrid catalysts for levulinic acid production from glucose. *Micropor. Mesopor. Mater.* **2013,** *171*, 14-23. DOI: https://doi.org/10.1016/j.micromeso.2013.01.002
29. Kumar, K.; Parveen, F.; Patra, T.; Upadhyayula, S., Hydrothermal conversion of glucose to levulinic acid using multifunctional ionic liquids: effects of metal ion co-catalysts on the product yield. *New J. Chem.* **2018,** *42* (1), 228-236. DOI: https://doi.org/10.1039/C7NJ03146G
30. Ramli, N. A. S.; Amin, N. A. S., Fe/HY zeolite as an effective catalyst for levulinic acid production from glucose: characterization and catalytic performance. *Appl. Catal. B* **2015,** *163*, 487-498. DOI: https://doi.org/10.1016/j.apcatb.2014.08.031
31. Qu, Y.; Zhao, Y.; Xiong, S.; Wang, C.; Wang, S.; Zhu, L.; Ma, L., Conversion of glucose into 5-hydroxymethylfurfural and levulinic acid catalyzed by SO_4^{2-}/ZrO_2 in a biphasic solvent system. *Energy Fuels* **2020,** *34* (9), 11041-11049. DOI: https://doi.org/10.1021/acs.energyfuels.0c01823
32. Pyo, S.-H.; Glaser, S. J.; Rehnberg, N.; Hatti-Kaul, R., Clean production of levulinic acid from fructose and glucose in salt water by heterogeneous catalytic dehydration. *ACS Omega* **2020,** *5* (24), 14275-14282. DOI: https://doi.org/10.1021/acsomega.9b04406

33. Wei, W.; Wu, S., Experimental and kinetic study of glucose conversion to levulinic acid in aqueous medium over Cr/HZSM-5 catalyst. *Fuel* **2018,** *225*, 311-321. DOI: https://doi.org/10.1016/j.fuel.2018.03.120
34. Weiqi, W.; Shubin, W., Experimental and kinetic study of glucose conversion to levulinic acid catalyzed by synergy of Lewis and Brønsted acids. *Chem. Eng. J.* **2017,** *307*, 389-398. DOI: https://doi.org/10.1016/j.cej.2016.08.099
35. Kumar, K.; Pathak, S.; Upadhyayula, S., 2nd generation biomass derived glucose conversion to 5-hydroxymethylfurfural and levulinic acid catalyzed by ionic liquid and transition metal sulfate: Elucidation of kinetics and mechanism. *J. Clean. Prod.* **2020,** *256*, 120292. DOI: https://doi.org/10.1016/j.jclepro.2020.120292
36. Wang, J.; Cui, H.; Wang, J.; Li, Z.; Wang, M.; Yi, W., Kinetic insight into glucose conversion to 5-hydroxymethyl furfural and levulinic acid in $LiCl{\cdot}3H_2O$ without additional catalyst. *Chem. Eng. J.* **2021,** *415*, 128922. DOI: https://doi.org/10.1016/j.cej.2021.128922
37. Kim, H. S.; Kim, S.-K.; Jeong, G.-T., Catalytic conversion of glucose into levulinic and formic acids using aqueous Brønsted acid. *J. Ind. Eng. Chem.* **2018,** *63*, 48-56. DOI: https://doi.org/10.1016/j.jiec.2018.01.038
38. Kumar, V. B.; Pulidindi, I. N.; Mishra, R. K.; Gedanken, A., Development of Ga salt of molybdophosphoric acid for biomass conversion to levulinic acid. *Energy Fuels* **2016,** *30* (12), 10583-10591. DOI: https://doi.org/10.1021/acs.energyfuels.6b02403
39. Upare, P. P.; Yoon, J.-W.; Kim, M. Y.; Kang, H.-Y.; Hwang, D. W.; Hwang, Y. K.; Kung, H. H.; Chang, J.-S., Chemical conversion of biomass-derived hexose sugars to levulinic acid over sulfonic acid-functionalized graphene oxide catalysts. *Green Chem.* **2013,** *15* (10), 2935-2943. DOI: https://doi.org/10.1039/C3GC40353J
40. Ramli, N. A. S.; Amin, N. A. S., Optimization of renewable levulinic acid production from glucose conversion catalyzed by Fe/HY zeolite catalyst in aqueous medium. *Energy Convers. Manag.* **2015,** *95*, 10-19. DOI: https://doi.org/10.1016/j.enconman.2015.02.013
41. Zhang, X.; Murria, P.; Jiang, Y.; Xiao, W.; Kenttämaa, H. I.; Abu-Omar, M. M.; Mosier, N. S., Maleic acid and aluminum chloride catalyzed conversion of glucose to 5-(hydroxymethyl) furfural and levulinic acid in aqueous media. *Green Chem.* **2016,** *18* (19), 5219-5229. DOI: https://doi.org/10.1039/C6GC01395C
42. Wei, W.; Yang, H.; Wu, S., Efficient conversion of carbohydrates into levulinic acid over chromium modified niobium phosphate catalyst. *Fuel* **2019,** *256*, 115940. DOI: https://doi.org/10.1016/j.fuel.2019.115940
43. Zhu, Q.-Q.; Zhuang, J.-P.; Wang, L.-Y.; Liu, Y.; Wu, S.-B., Silicotungstate: An inexpensive and efficient catalyst for conversion of glucose to levulinic acid in aqueous medium. *J. Biobased Mater. Bioenergy* **2019,** *13* (5), 677-682. DOI: https://doi.org/10.1166/jbmb.2019.1906
44. Liu, Y.; Li, H.; He, J.; Zhao, W.; Yang, T.; Yang, S., Catalytic conversion of carbohydrates to levulinic acid with mesoporous niobium-containing oxides. *Catal. Commun.* **2017,** *93*, 20-24. DOI: https://doi.org/10.1016/j.catcom.2017.01.023